RSC Advances

PAPER

View Article Online
View Journal | View Issue

Cite this: *RSC Adv.*, 2022, **12**, 18115

Understanding of physicochemical properties and antioxidant activity of ovalbumin–sodium alginate composite nanoparticle-encapsulated kaempferol/tannin acid†

Xiaoya Tao, ‡[ab] Hang Shi,‡[c] Ailing Cao*[d] and Luyun Cai *[a]

In this research, ovalbumin (OVA) and sodium alginate (SA) were used as the materials to prepare an OVA–SA composite carrier, which protected and encapsulated the hydrophobic kaempferol (KAE) and the hydrophilic tannic acid (TA) (OVA–SA, OVA–TA–SA, OVA–KAE–SA, and OVA–TA–KAE–SA). Results showed that the observation of small diffraction peaks in carriers proved the successful encapsulation of KAE/TA. The protein conformation of the composite nanoparticles changed. OVA–TA–SA composite nanoparticles had the highest α-helix content and the fewest random coils, so the protein structure of it had the strongest stability. OVA–TA–KAE–SA composite nanoparticles had the strongest system stability and thermal stability, which might be due to the synergistic effect of the two polyphenols, suggesting the encapsulation of KAE/TA increased the system stability and the thermal stability of OVA–SA composite nanoparticles. Additionally, the composite nanoparticles were endowed with antioxidant ability and antibacterial ability (against *Staphylococcus aureus* and *Escherichia coli*) in the order OVA–TA–SA > OVA–TA–KAE–SA > OVA–KAE–SA based on the difference in antibacterial diameter (*D*, mm) and square (*S*, mm^2), indicating that polyphenols enhanced the antibacterial and antioxidant ability of OVA–SA composite nanoparticles, and the enhancement effect of TA was stronger than that of KAE. These results provide a theoretical basis for the application of OVA–SA composite nanoparticles in the delivery of bioactive compounds.

Received 28th April 2022
Accepted 9th June 2022

DOI: 10.1039/d2ra02708a

rsc.li/rsc-advances

1. Introduction

Nanocarriers function as potential delivery carriers for drugs, as well as healthy and nutritional products, owing to their ability to penetrate biofilm barriers.[1] Also, they have been shown to protect the entrapped components from enzymatic attack, and provide controlled release rates and targeted delivery.[2] Nanoparticle polymer-carriers improve the water solubility and oral bioavailability of their core molecules. Protein, an amphiphilic biopolymer, has been regarded as an ideal material for the preparation of nano-sized delivery carriers based on the low toxicity and the ability to encapsulate bioactive substances and solvents,[3,4] and is usually thermally treated to improve its surface hydrophobicity for the binding of lipophilic molecules.[5]

Ovalbumin (OVA), a typical good-quality globulin in egg white protein, is highly soluble in water, easily digestible, self-assembling, amphiphilic; and acts as a lipophilic and efficient carrier owing to the hydrophobic and charged amino acids.[6] OVA can interact with food components by electrostatic, hydrophobic and hydrogen bonding forces,[6] and it has been widely used to prepare nanoparticles for the delivery of bioactive compounds, such as curcumin[5] and polyunsaturated fatty acids,[7,8] to improve water solubility, stability, and antioxidant activity. The report has shown that encapsulation in egg white protein nanoparticles protects the antioxidant activity and effectiveness of curcumin.[9] Also, the study of a dual fluorescence reverse targeting drug delivery system based on curcumin–OVA nanoparticles for allergy treatment provides a theoretical basis for the application of OVA as an embedding carrier.[10] The noncovalent interactions of OVA with polysaccharides or polyphenols can influence its structure and interfacial properties.[11] Thus, it is necessary to analyze the interaction between OVA and other food molecules. Sodium alginate (SA), an anionic polysaccharide extracted from the cell walls of seaweeds,[12] can promote the stability of a protein or

[a]*Ningbo Research Institute, College of Biosystems Engineering and Food Science, Zhejiang University, Ningbo, 315100, China. E-mail: cailuyun@zju.edu.cn; Fax: +86 571 88982726; Tel: +86 571 88982726*

[b]*Institute for Innovative Development of Food Industry, Institute for Advanced Study, Shenzhen University, Shenzhen, 518060, China*

[c]*College of Food Science and Engineering, Bohai University, Jinzhou, 121013, China*

[d]*Hangzhou Customs District, Hangzhou, 310007, China. E-mail: caoailing2002@163.com*

† Electronic supplementary information (ESI) available. See https://doi.org/10.1039/d2ra02708a

‡ These authors contributed equally to this work.

protein-stabilized vehicles and reduce their hydrolysis during digestion.[13,14] Conjugation of curcumin onto alginate enhanced aqueous solubility and stability of curcumin.[15] A report showed the mechanical, rheological and structural properties of fiber-containing microgels based on whey protein and alginate.[16] Sodium caseinate–sodium alginate-stabilized zein nanoparticles improved the water solubility, photochemical stability and antioxidant activity of curcumin.[1] Kaempferol (KAE) is a natural polyphenol flavonoid that has anti-inflammatory and antioxidative effects, and it has been used in the prevention and treatment of osteoporosis, diabetes, and atherosclerosis, as well as the protection of the liver, nerves, and myocardium.[17] However, KAE degrades rapidly in an aqueous solution because of its poor solubility. Thus, nano-encapsulation can be an effective way to improve the solubility of KAE by providing a closed microenvironment. Tannic acid (TA), a common polyphenol compound, shows unique biological activities and physicochemical properties, and plays an important role in drug delivery, surface modification, and prepared other materials.[18,19] TA can interact with proteins through hydrogen bonds, coordination, or hydrophobic interactions.[20,21] Reports have shown that the protein interactions with polyphenol enhance its functional properties by changing the structural characteristics.[22–24] For example, OVA can bind TA well to improve its stability and reduce its emulsifying ability.[6] The emulsifying ability of OVA stabilized emulsions decreased after binding with TA owing to the reduction in interfacial activities, additionally, TA reduced the emulsion stability.[25]

Study showed that OVA and SA could be used as the building blocks to encapsulate curcumin to improve the stability, bioaccessibility, and antioxidant activity.[26] OVA and SA used to develop protein–polysaccharide complexes had excellent stability and great sustained-release performance for VD_3, contributing to the digestion and absorption of vitamin by human body.[27] Also, report showed that sacha inchi oil was microencapsulated *via* complex coacervation of OVA and SA/TA to improve the thermal behavior of microcapsules.[28,29] Zhang *et al.*[30] showed that OVA–SA coacervates could be used as a novel Pickering stabilizer in the food industry. To date, information about OVA–SA composite carrier to protect and encapsulate the hydrophobic KAE and the hydrophilic TA is obscure. Thus, this study aimed to analyze the physicochemical properties and antioxidant activity of OVA–SA composite nanoparticles encapsulated KAE/TA, which will provide a theoretical basis for the application of OVA–SA composite nanoparticles in the delivery of bioactive compounds. The flow diagram of this study is shown in ESI Fig. S1.†

2. Materials and methods

2.1. Materials

Ovalbumin (OVA, albumin from chicken egg white, nitrogen content ≥ 12.5%, total protein on a dry basis ≥ 80%, relative molecular mass less than 1000 ≥ 80%, pI: 4.43–4.66; purity ≥ 80%), sodium alginate [SA, viscosity, 10 g L^{-1}, 20 °C, (Pa s) ≥ 0.02], LB broth, LB nutrient agar, 1,1-diphenyl-2-picrylhydrazyl (DPPH), 2,2′-azino-bis(3-ethylbenzothiazoline-6-sulfonic acid) diammonium salt (ABTS), and water-soluble vitamin E Trolox were purchased from Solarbio Technology Co., Ltd. (Beijing, China). Kaempferol (KAE, a polyphenol from brown algae, purity ≥ 97%), tannic acid (TA), potassium persulfate, potassium ferricyanide, and iron(III)chloride anhydrous were purchased from Aladdin Biochemical Technology Co., Ltd. (Shanghai, China). The Folin-phenol reagent was purchased from Bomei Biotechnology Co., Ltd. (Hefei, China). All other chemicals used were analytical grade, and purchased from Sinopharm Chemical Glass Co., Ltd. (Jinzhou, China).

2.2. The preparation of OVA–SA composite nanoparticles

All solutions were freshly prepared for immediate use. OVA nanoparticle suspension was prepared by the reverse solvent method.[9] 10 g L^{-1} OVA solution and SA solution were prepared using deionized water, stirred for 2 h at room temperature, and then placed in a refrigerator overnight (4 °C) to ensure adequate hydration. To obtain OVA–SA nanoparticle suspension, OVA solution and SA solution was fully mixed in the ratio of 5 : 2 (w/w), which was determined by optimizing the results of preliminary experiments. After stirred for 2 h at room temperature, the mixture was placed in a stoppered glass bottle, heated in a water bath at 80 °C for 1 h, and then kept at 4 °C for further use.

2.3. Encapsulation of kaempferol and tannin acid

All solutions were freshly prepared for immediate use. Generally, KAE or TA was dissolved in 70% ethanol or deionized water using an ultrasonic processor (KQ-400KDE, Kunshan Ultrasonic Instrument Co., Ltd., China) respectively. The prepared KAE or/and TA solution was added to OVA nanoparticle suspension and stirred vigorously for 30 min, and then they were mixed with SA solution. After stirred for 3 h, the mixture was heated in a water bath at 80 °C for 30 min. The obtained composite nanoparticles were referred to as OVA–SA–TA, OVA–KAE–SA, and OVA–KAE–TA–SA. The final products were freeze-dried before the further use. The ratio of the composite nanoparticles above is as follows: OVA : polyphenol = 5 : 3 (w/w), OVA : SA = 1 : 1.5 (v/v). The ratios above were determined by optimizing the results of preliminary experiments.

2.4. Determination of particle size and zeta potential

The nanoparticle samples were dispersed in Milli-Q water before the analysis to avoid multiple scattering effects.[31] The particle size and zeta potential of nanoparticle samples (0.1 g L^{-1}) were determined using a nanoparticle size analyzer (90Plus, Brookhaven Instruments Corporation, USA) at room temperature.

2.5. Determination of UV spectra

The sample was diluted to 0.1 g L^{-1} using deionized water. With deionized water as a blank control, the sample was scanned at a speed of 2 nm s^{-1} under a wavelength of 190–600 nm with a resolution of 0.5 nm.

2.6. Determination of endogenous fluorescence

Sample solutions with 0.1 g L^{-1} protein contents were prepared and analyzed by a fluorescence spectrophotometer (970 CRT, Precision Scientific Instrument Co., Ltd., China). With the fluorescent group in OVA molecule as a probe, the slit widths of excitation light and emission light were 10 nm and 5 nm respectively. The excitation wavelength and the emission wavelength were 295 nm and 295–500 nm respectively.[32]

2.7. Determination of Fourier transform infrared spectroscopy (FTIR)

The secondary structure of the samples was analyzed using Fourier transform infrared spectroscopy (FTIR) (Scimitar 2000, Agilent Technologies Inc., USA) according to the previous method.[22] Generally, 1 mg of lyophilized sample was mixed with 100 mg of dried KBr and ground into fine powder. Afterwards, the powder sample was formed into a sheet and scanned in the sample chamber. The wave number range was 4000–500 cm^{-1} with a resolution of 2 cm^{-1}. The obtained data were analyzed using OMNIC 8.2 (Thermo Fisher Scientific Inc., USA).

2.8. Determination of differential scanning calorimetry (DSC)

The differential scanning calorimetry (DSC) was determined based on the previous method[33] with little modifications. The heat shrinkage temperature and thermal enthalpy of the samples were measured using a differential scanning calorimeter (Q2000, TA Instruments, USA). 10 mg of freeze-dried sample was placed in an aluminum pan, keeping good contact with the pan bottom, and an empty aluminum pan was used as a reference. The heating temperature ranged from 20 °C to 200 °C at a rate of 5 °C min^{-1}. The denaturation temperature and converted enthalpy were assessed by TA Universal Analysis software (TA Instruments, USA).

2.9. Determination of X-ray diffraction (XRD)

The crystal structure of the samples was analyzed using an X-ray diffraction instrument (Ultima IV, Rigaku Corporation, Japan). The lyophilized powder sample was placed on a silicon wafer to measure the indicator, and the scan range was changed from 5 to 80° (2θ) at a speed of 10° min^{-1} with CuK^{+} radiation.[34] The tube current and operating voltage of the X-ray generator were 40 mA and 40 kV, respectively. The obtained results were qualitatively analyzed by comparing the diffraction peak positions of the samples.

2.10. Rheological properties measurements

Rheological properties were conducted using a rotational rheometer (Discovery HR-1, TA Instruments, USA) with a parallel plate (diameter 40 mm, gap 1 mm). The measurements were performed in the range of strains from 0.1 to 100% at 1 Hz frequency at 25 °C.

2.11. Determination of polyphenol binding equivalent by Folin-phenol method

0.2 g L^{-1} KAE/TA standard solution was prepared and then diluted to different concentrations. 1 mL of each solution was thoroughly mixed with 1 mL of 0.25 M Folin phenol reagent, and allowed to stand for 3 min. Afterwards, 2 mL of 15% Na_2CO_3 solution was added to the mixture above, then thoroughly shaken, and lastly allowed to stand for 30 min. With 15% Na_2CO_3 solution as a blank control, the absorbance was measured at 760 nm (ref. 35) using a UV spectrophotometer (UV-2550, Unico Instrument Co., Ltd., China), and a polyphenol standard curve was drawn. Similarly, the absorbance of 1.0 g L^{-1} sample solution was measured and the polyphenol content in the samples was analyzed according to the polyphenol standard curve.

2.12. Determination of antioxidant activity

2.12.1. DPPH free radical scavenging activity. Prior to the experiment, solutions of 0.05 g L^{-1} DPPH in anhydrous ethanol and 50 μM Trolox solution were prepared. Trolox solution was diluted with anhydrous ethanol into a series of solutions (40, 35, 30, 25, 20, 10, and 5 μM). The experimental group (2 mL DPPH + 2 mL test sample), the control group (2 mL anhydrous ethanol + 2 mL test sample), and the blank group (2 mL DPPH + 2 mL anhydrous ethanol) were also prepared. The reaction mixture was kept in darkness for 30 min at room temperature. The absorbance of the samples was measured at 517 nm, and the result was presented as μmol Trolox per g.[36]

2.12.2. $ABTS^{+}$ free radical scavenging activity. The reaction mixture consisting of 7 mM ABTS in anhydrous ethanol and 2.5 mM $K_2S_2O_4$ (1 : 1, v/v) was kept in the dark for 16 h at room temperature to form the $ABTS^{+}$ radical stock solution. Afterwards, the stock solution was diluted with anhydrous ethanol into a working solution ($ABTS^{+}$) with the absorbance of 0.70 ± 0.02 at 734 nm for subsequent use. Then, the experimental group (1 mL $ABTS^{+}$ + 3 mL test sample), the control group (1 mL anhydrous ethanol + 3 mL test sample), and the blank group (1 mL $ABTS^{+}$ + 3 mL anhydrous ethanol) were prepared. The reaction mixture was kept in darkness for 30 min at room temperature. The absorbance of the samples was measured at 734 nm, and the result was expressed as μmol Trolox per g.[2]

2.12.3. Evaluation of reducing ability (potassium ferricyanide method). 1 mL of sample (0.1 g L^{-1} in anhydrous ethanol) was thoroughly mixed with 2.5 mL of 0.2 M PBS (pH 6.6) and 2.5 mL of 1% potassium ferricyanide. Afterwards, the mixture was reacted in a water bath at 50 °C for 20 min and cooled in a 4 °C refrigerator. Then, 2.5 mL of 10% trichloroacetic acid was added to the reaction mixture. After shaken well, 2.5 mL of the mixture above was mixed with 2.5 mL of ultrapure water and 0.5 mL of 0.1% ferric chloride to react for 15 min at room temperature. The absorbance was measured at 700 nm, and the result was expressed as μmol Trolox per g.[37]

2.13. Determination of antibacterial activity

The strains [*Staphylococcus aureus* (ATCC6538) and *Escherichia coli* (ATCC8739)], kept at −80 °C in a cryo-preservative solution,

were inoculated in LB broth medium at an ultra-clean table, and incubated overnight at 37 °C in a constant temperature incubator. Afterwards, a second inoculation was performed at 37 °C for 12 h to obtain freshly cultured microbial suspensions. Antibacterial activity testing was carried out using the agar diffusion method. The prepared second-generation strains were added into the sterile LB nutrient agar, and the amount of the strains added was 0.1% of LB nutrient agar. After fully shaken, 25 mL of the strains was poured into a sterile Petri dish with an Oxford cup ($d = 7.5$ mm), making the inoculum density in the test plate 10^6 CFU mL^{-1}. The Oxford cup was taken out after LB nutrient agar solidified, and then 100 μL of the prepared samples was added into the hole. After stood at 4 °C for 4 h, the plates were placed at 37 °C for constant temperature inversion for 24 h. Lastly, the diameter of the inhibition zone was measured, and the area was calculated.

2.14. Statistical analysis

All experiments were performed in triplicate, and the result was expressed as mean ± standard deviation (SD). Data were analyzed using SPSS 22.0 (SPSS Inc., USA) and analysis of variance (ANOVA), and differences at $P < 0.05$ were considered as statistically significant when the means were compared by Duncan multiple range test. All figures were plotted using OriginPro 9.0 (OriginLab Co., USA).

3. Results and discussion

3.1. Particle diameter and zeta-potential

Both particle diameter and zeta-potential are critical characteristics in predicting the stability of protein nanoparticles and their efficacy in biomedical applications. The changes in particle size and zeta-potential of four composite nanoparticles were shown in Fig. 1A and B. Generally, the particle sizes of OVA–SA became larger after loading with polyphenols. The ζ and effective particle sizes of OVA–SA, OVA–TA–SA, OVA–KAE–SA, and OVA–TA–KAE–SA were −56.87, −37.20, −30.20, and −46.17 mV, and 167, 291, 323, and 207 nm, respectively. Among them, OVA–SA had the largest |ζ| value and the smallest particle size, indicating that OVA–SA delivery system had the best stability. Previous reports showed that a larger |ζ| value (higher than 30 mV or lesser than −30 mV) indicated more charges on the surface of a protein molecule, which suggested a stronger repulsive force between molecules in solution, contributing to a stable system.[38] Therefore, protein aggregation was suppressed, and the lower effective particle size indicated higher system stability. The encapsulation efficiency of the delivery systems is highly related with the surface hydrophobicity and specific surface area,[5] and also the tertiary conformation of proteins.[39] When the aggregation of protein was inhibited, more hydrophobic binding sites were available for bioactive component, which will contribute to a high encapsulation efficiency. The SA chain stretched during the self-assembly process of OVA and SA, which contributed to the exposure of more charged groups and the increase in the charge on the particle surface, indicating that OVA–SA nanoparticle system is stable. Additionally, the effective particle size and the |ζ| value of OVA–SA nanoparticles loaded with KAE/TA were smaller and larger than that of OVA loaded with KAE/TA (unpublished data) respectively, suggesting that the addition of SA inhibited the aggregation of OVA and enhanced the stability of the nanoparticle system;[40] however, OVA–SA nanoparticles loaded with KAE and TA together were more stable than the single-loaded KAE/TA composite nanoparticle system due to the smaller particle size and the larger |ζ| value, indicating that the assembly effect of OVA–TA–KAE–SA was better. The result was consistent with a higher encapsulation efficiency due to the slight increase in particle size, which was in accordance with the reports by Feng *et al.*[26] and Zhou *et al.*[41]

3.2. UV absorption spectra

A certain organic compound introduces a group containing an unshared electron pair due to a reaction, which causes the absorption peak to shift to a long wavelength called a long shift or red shift. In contrast, shift to a reverse short wavelength is called a short shift or blue shift. The increase of the absorption intensity is called the dense color effect or the hyperchromic effect, whereas the decrease is called the light color effect.[42] The UV absorption spectra of different composite nanoparticles were shown in Fig. 1C. A strong absorption peak was observed in the wavelength range of 260–360 nm, indicating that the molecular structure of the composite nanoparticle contained ≥3 conjugated double bonds.[43] The OVA–SA composite nanoparticle contained an obvious absorption peak at 274 nm, which was due to the presence of aromatic amino acids with conjugated double bonds such as tyrosine and phenylalanine in OVA.[44] Additionally, the absorption intensity of OVA–TA–SA was higher than that of OVA–SA, because the characteristic absorption peak of the benzene ring in the TA structure was enhanced and overlapped with the OVA absorption peak. The OVA–KAE–SA composite nanoparticle had characteristic absorption peaks at 262 nm and 362 nm, and the absorption peak was strong at 362 nm, which was due to the fact that KAE contained more than 3 strong conjugated double bonds. OVA–TA–KAE–SA composite nanoparticle had a absorption peak at around 360 nm, and the absorption intensity was reduced and the red shift occurred compared with OVA–KAE–SA composite nanoparticle, which was due to the reason that the loading of the hydrophilic TA weakened the structural change of the hydrophobic KAE on the composite carrier, and the acidity of TA changed the pH of the composite nanoparticle solution,[45] resulting in the reduction in the energy difference between the energy levels, as well as the electron transition energy. The conjugation effect of OVA–TA–KAE–SA composite nanoparticle conferred the absorption redshift. The result is consistent with the fact that polyphenols exhibit good resistance to UV radiation.[46] Additionally, the observation of the absorption peak at 272 nm was due to the $n \rightarrow \pi^*$ energy level transition of the organic chromophore C=O in the composite nanoparticle structure.[47] The results of UV absorption spectra showed that the combination of OVA–SA nanoparticles and KAE/TA changed

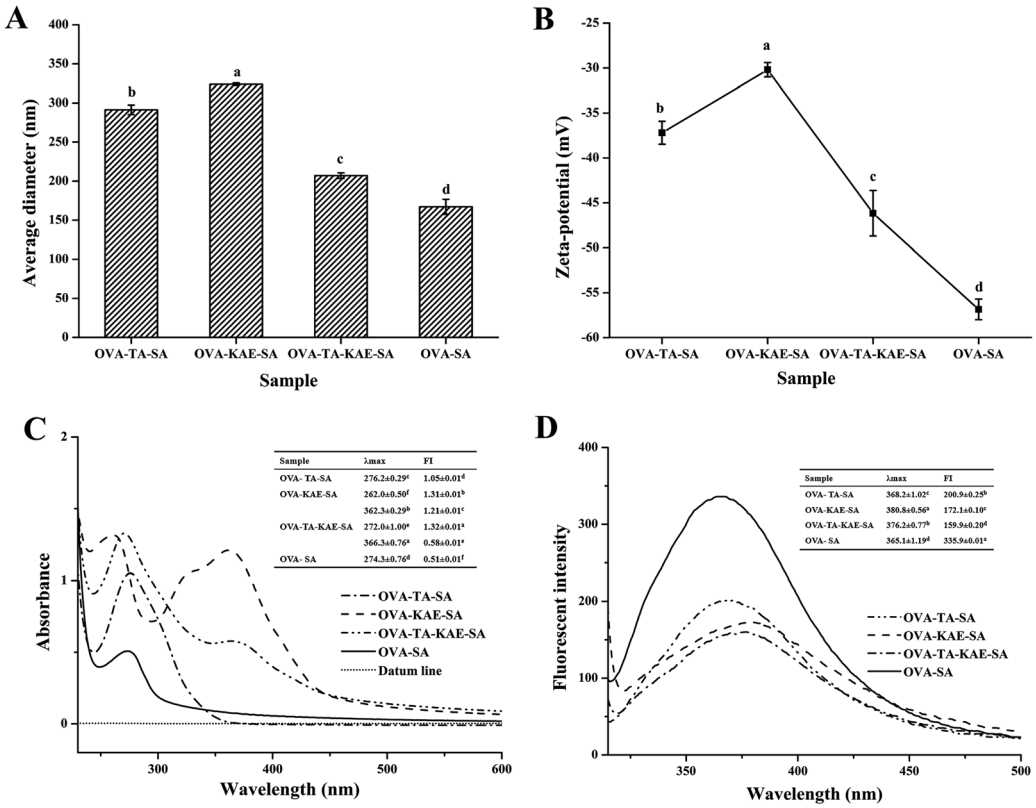

Fig. 1 Changes in average diameter (A) and zeta potential (B), UV absorption spectra (C) and intrinsic fluorescence spectra (D) of OVA–SA composite nanoparticles encapsulated KAE/TA. Values are expressed as mean ± standard deviation. Different letters in the same column indicate significant differences at $P < 0.05$.

the protein conformation of OVA–SA nanoparticles in different varying degrees.

3.3. Fluorescence spectra

The fluorescence spectra of different composite nanoparticles were shown in Fig. 1D. The fluorescence absorption peaks of the composite nanoparticles were observed between 365–380 nm. After OVA–SA was loaded with KAE/TA, the fluorescence was accompanied by a red shift from 365 nm to 380 nm, and the degree of red shift was as follows: OVA–KAE–SA > OVA–TA–KAE–SA > OVA–TA–SA > OVA–SA. The result was due to the reason that OVA–SA nanoparticles were embedded the hydrophobic polyphenol KAE/hydrophilic polyphenol TA, different degrees of protein denaturation occurred, resulting in the gradual exposure of aromatic amino acids molecular side chain groups to water and the polarity of the environment.[48] Similarly, OVA (with a fluorescence absorption peak of 356 nm) also had a red shift after combining with SA to form protein–polysaccharide nanoparticles, and the red shift reflected the degree of protein conformation change. Additionally, KAE and TA contained a large number of aromatic rings and phenolic hydroxyl groups. As the number and the fusion degree of aromatic rings increased, λ_{max} had a red shift. Compared with OVA nanoparticles loaded with KAE/TA (unpublished data), OVA–SA nanoparticles had smaller changes in protein conformation, which further showed that SA and KAE/TA acted together to weaken the change degrees of OVA protein conformation. A previous study also found that the encapsulation of curcumin in zein/caseinate/SA nanoparticles showed a similar result.[1]

3.4. FTIR

FTIR can determine the molecular structure of composite nanoparticles and study the interaction between different components of composite nanoparticles. Fig. 2A shows the infrared spectra of different composite nanoparticles, and Table 1 corresponds to the peak positions and spectra analysis. When OVA–SA was loaded with KAE/TA, the polarity of the bond formed between KAE/TA and OVA–SA was different, and the FTIR strength increased with the increase of polarity; additionally, the molecular group of KAE/TA had different conjugation conditions with the electron withdrawing group and the electron donating group. Generally, the molecular group was conjugated with the electron withdrawing group, the vibration frequency increased, otherwise the vibration frequency decreased.[49] Table 1 showed that OVA–SA composite nanoparticles loaded with KAE/TA had characteristic infrared absorption peaks, including amides I (around 1650 cm^{-1}), II (around 1300–1500 cm^{-1}), and III (around 1250 cm^{-1}), along

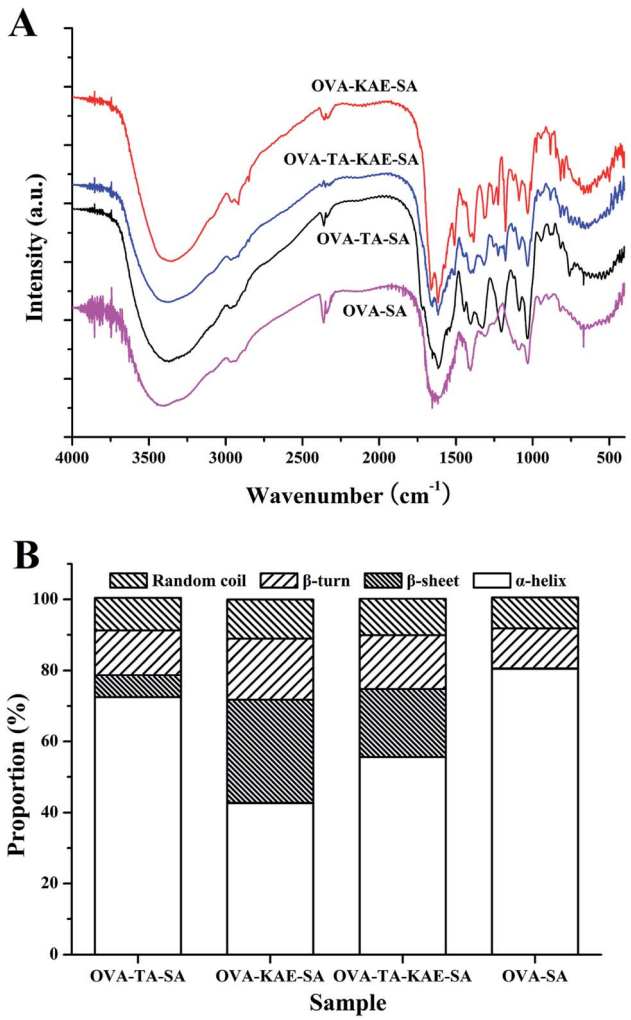

Fig. 2 Infrared spectra (A) and secondary structure content (B) of OVA–SA composite nanoparticles encapsulated KAE/TA.

with A (3300–3400 cm^{-1}) and B (about 2800–2900 cm^{-1}) bands, and they all had different degrees of blue shift, indicating that KAE/TA reacted with the phenolic hydroxyl groups in OVA–SA nanoparticles. The four composite nanoparticles all showed broad peaks between 3300–3400 cm^{-1}, which were due to the –NH stretching vibration in the amide A band. The amide B band was due to the asymmetric stretching vibration caused by –CH.[50] Amide I and II bands mainly reflect the bending vibration and stretching vibration of the peptide backbone.[51]

Amide I band is more sensitive to the changes and the quantitation of protein secondary structure.[52,53] In this study, Gaussian line function fitting was performed on the I band of the infrared spectrum through second-order derivation, deconvolution and curve iterative fitting, as shown in ESI Fig. S2.† As shown in Fig. 2B, the content of protein secondary structure of different composite nanoparticles was calculated based on the comparison of the corresponding peak areas of different secondary structures in the amide I region. The contents of α-helix, β-sheet, β-turn, and random coils of OVA–SA were 80.48%, 0.10%, 11.24%, and 8.73%, respectively. Compared with OVA–SA, the α-helix content of OVA–TA–SA, OVA–KAE–SA, and OVA–TA–KAE–SA decreased by 7.15%, 37.74%, and 24.88%, and the random coils content increased by 0.54%, 2.31%, and 1.52%, as well as the β-sheet content increased greatly, indicating that binding of hydrophobic polyphenol KAE increased the protein folding of OVA, and contributed to a clear transformation from α-helix to β-sheet of OVA–SA.[40] The result was supported by the report that some α-helical chain structures of zein were unravelled by breaking hydrogen bonds, accompanying with the realignment and reorganization into a β-sheet conformation.[54] The phenomenon can be assumed that hydrogen bonds of α-helix and β-sheets may be broken during incubation, contributing to the formation of random coils, which may provide complexation sites for TA to interact.[40,55] After OVA–SA was loaded with KAE/TA, the α-

Table 1 Location and assignment of the peaks identified in FTIR spectra for encapsulation of KAE/TA in OVA–SA composite nanoparticle

Region	Peak wavenumber (cm^{-1})				Assignment and remarks
	OVA–SA	OVA–TA–SA	OVA–KAE–SA	OVA–TA–KAE–SA	
Amide A	3400	3383	3375	3381	N–H stretch coupled with hydrogen bond
Amide B	2973	2951	2962	2955	C–H antisymmetric and symmetric stretching
	2873	—	2864	—	C–H antisymmetric and symmetric stretching
Amide I	1650	1653	1661	1662	C=O Stretch/hydrogen bond coupled COO^-
Amide II	1519	1530	1514	1514	NH bend coupled with CN stretch
	1408	1412	1405	1409	CH_2 bending (scissors) vibration
	1311	1329	1310	1313	CH_2 wag of proline and glycine
Amide III	1131	1198	1178	1172	NH bend stretch coupled C–N stretch
Fingerprint	1042	1038	1035	1033	C–O skeletal stretch
	945	947	940	949	C–H deformation vibration (carbohydrate)
	825	872	883	884	C–H deformation vibration (carbohydrate)
	670	666	660	663	C–C skeletal stretch

helix content of OVA–TA–SA was the highest, and the random coil was the lowest, indicating that its protein structure had the strongest stability and the best integrity, followed by OVA–TA–KAE–SA and OVA–KAE–SA.

3.5. DSC analysis

DSC is a commonly used thermodynamic analysis method. The thermal denaturation temperature (T_m) can directly reflect the thermal stability of proteins, and the enthalpy (ΔH) can be obtained by calculating the peak area corresponding to T_m.[56] The DSC scanning curves of the composite nanoparticles were shown in Fig. 3. T_m and ΔH of each composite nanoparticle in Fig. 3 were described in Table 2. The composite nanoparticles all contained two absorption peaks, and the area of the second absorption peak was much larger than that of the first absorption peak, indicating that the change of the thermal energy in the composite nanoparticles was mainly above 100 °C. Generally, T_m of OVA–SA composite nanoparticles loaded with KAE/TA was 0.2–16 °C higher than that of OVA–SA composite nanoparticles, indicating that the loading of KAE/TA enhanced the oxidation resistance and thermal stability of OVA–SA composite nanoparticle. The larger ΔH of OVA–SA and OVA–KAE–SA composite nanoparticles indicated that the dimensional structural stability was higher, thus more energy was needed to break the spatial structure of the nanoparticles.[57] Additionally, Table 2 showed that the T_m value of OVA–TA–KAE–SA was 149.34 °C, which was the highest among the four nanoparticles. The result may be due to the reason that the thermal stability of KAE and TA acts synergistically accompanying with OVA–SA loading together, and also that KAE and TA enhance the antioxidant capacity of OVA–SA, which suggests OVA–SA has a better embedding effect on KAE and TA.

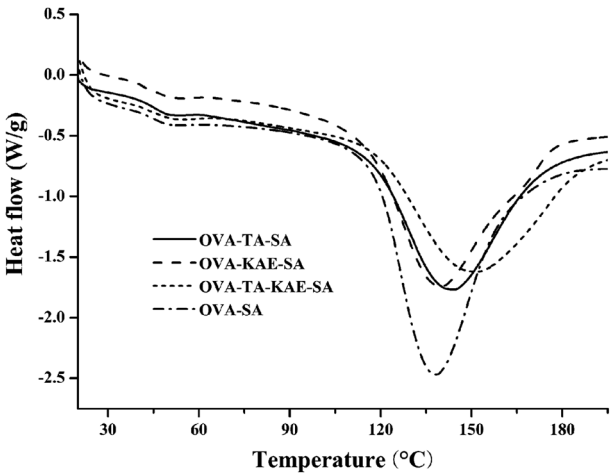

Fig. 3 The changes in DSC scanning curve of OVA–SA composite nanoparticles encapsulated KAE/TA.

3.6. XRD analysis

X-ray powder diffractometer can reflect the bulk information structure of composite nanoparticles. XRD scanning curves of different composite nanoparticles were shown in Fig. 4. The four composite nanoparticles contained two broad diffraction peaks. The first broad diffraction peak was located at about $2\theta = 5.6$, which was the first large diffraction peak presented by OVA as the coating wall material, indicating it had an ordered structure, and the second broad diffraction peaks were located at $2\theta = 22.92$, 22.0, 21.74, and 21.04 for OVA–TA–SA, OVA–KAE–SA, OVA–TA–KAE–SA, and OVA–SA respectively. According to the Bragg's law $d(\text{Å}) = \lambda/2 \sin\theta$ ($\lambda = 1.54$ Å), the corresponding interplanar spacing d values were 3.88 Å, 4.04 Å, 4.08 Å, and 4.23 Å. The reaction between SA and OVA changed the protein conformation of OVA, resulting in the second large diffraction peak of the composite nanoparticle shifted to different degrees. Additionally, the change of the interplanar spacing d was the result of the good combination of SA and OVA.

The crystallinity of the four composite nanoparticles was very low, and the basic carrier hindered the crystallization of polyphenols and promoted the formation of amorphous structures during the embedding process, which were in agreement with the report that Fe–TA alloy films had a crystalline to amorphous phase transition when TA was adding.[58] The XRD pattern of TA from XRD crystal database-Cambridge Crystal Data Center (CCDC) showed that the diffraction peaks of TA were at $2\theta = 8$, 10, 11, 21, 25, 26, 27, 28, 29, *etc.*, which were crystal characteristics. Similarly, KAE also had the rich and fine peak structures.[59] The results were in contrast to the large and broad peaks exhibited by OVA–SA composite nanoparticles, which indicated that KAE and TA were embedded in OVA–SA composite nanoparticles with an amorphous form. Several small diffraction peaks at $2\theta = 9.04$, 10.12, 15.18, 31.34, and $2\theta = 9.18$, 15.28 respectively were observed in OVA–KAE-SA and OVA–TA–KAE–SA composite nanoparticles, whereas they were not observed in

Table 2 Thermal denaturation midpoint temperature (T_m) and enthalpy (ΔH) of OVA–SA composite nanoparticles encapsulated KAE/TA[a]

	Peak 1		Peak 2	
Sample	T_m (°C)	ΔH (J g^{-1})	T_m (°C)	ΔH (J g^{-1})
OVA–TA–SA	49.94 ± 0.26^{a}	2.65 ± 0.25^{a}	137.25 ± 1.39^{b}	162.13 ± 0.25^{b}
OVA–KAE–SA	50.66 ± 0.43^{a}	3.09 ± 0.37^{a}	136.82 ± 2.37^{bc}	196.60 ± 14.85^{a}
OVA–TA–KAE–SA	50.20 ± 0.96^{a}	3.09 ± 0.32^{a}	149.34 ± 2.99^{a}	162.83 ± 26.82^{b}
OVA–SA	49.71 ± 0.79^{a}	3.04 ± 0.67^{a}	133.03 ± 0.37^{c}	202.77 ± 7.68^{a}

[a] Values are expressed as mean ± standard deviation. Different letters in the same column indicate significant differences at $P < 0.05$.

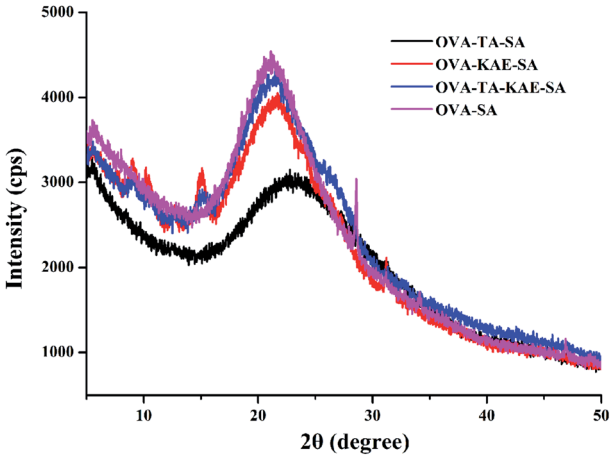

Fig. 4 The changes in XRD scanning curves of OVA–SA composite nanoparticles encapsulated KAE/TA.

OVA–TA–SA composite nanoparticle, suggesting that OVA–TA–SA had the best capsulated effect by OVA–SA composite nanoparticle, followed by OVA–TA–KAE–SA and OVA–KAE–SA.

3.7. Rheological properties

As shown in Fig. 5, the viscosity and shear force of four composite nanoparticle solutions changed accompanied with shear rate. The shear force of the four composite nanoparticles greatly increased along with the increase in shear rate. The shear force in different composite nanoparticles was OVA–KAE–SA > OVA–TA–KAE–SA > OVA–SA > OVA–TA–SA, and it changed little at a shear rate of 10^{-1} to 10 s^{-1}, whereas it increased exponentially at a shear rate of 10–100 s^{-1}. The viscosity of OVA–KAE–SA was much greater than that of OVA–TA–KAE–SA, and the viscosity of them decreased as the shear rate increased until the molecular arrangement of the composite nanoparticles remained unchanged, which was a shear thinning and pseudoplastic fluid.[60] Whereas the viscosity of OVA–SA and OVA–TA–SA was relatively low, and it slightly increased with the increase of shear force, which was a swelling plastic fluids.[33] The OVA molecules in the four composite nanoparticles were gradually ordered with the gradual increase of the shear rate. When the shear rate reached a certain value, the intermolecular arrangement was completed and the viscosity was gradually stabilized. The loading of KAE and TA had significantly different effects on the viscosity of OVA–SA composite nanoparticles, and the loading of KAE greatly increased the viscosity of OVA–SA composite nanoparticles.

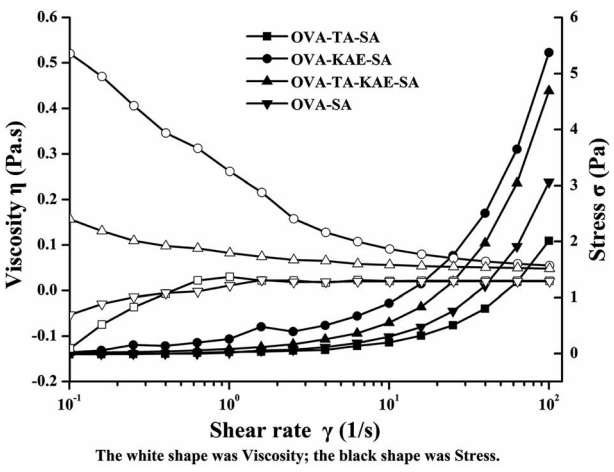

Fig. 5 The changes in viscosity and shear force (*C*) of OVA–SA composite nanoparticles encapsulated KAE/TA.

3.8. Polyphenol content and antioxidant activity

The polyphenol content of composite nanoparticles was determined by Folin-phenol method, and the result was expressed based on protein as mg g^{-1}. DPPH, $ABTS^{+}$ free radical scavenging ability, and Fe reducing ability were measured, and the results were expressed as Trolox equivalent. Total phenol content and antioxidant activity of different composite nanoparticles were shown in Fig. 6. For OVA–TA–SA, OVA–KAE–SA, and OVA–TA–KAE–SA, the phenol content was 387.09, 392.71, and 415.81 mg g^{-1}, DPPH free radical scavenging ability was 4868.5, 2391.8, and 3592.9 μmol Trolox per g, $ABTS^{+}$ scavenging ability was 2236.5, 1313.1, and 1814.7 μmol Trolox per g, and Fe reducing ability was 1185.2, 882.9, and 1290.0 μmol Trolox per g. These results showed that OVA–TA–SA had the strongest antioxidant activity, while its phenol content was not the most, indicating that OVA–SA had the best embedding effect to improve the bioavailability of TA, which can effectively scavenge free radicals and protect the body.[61] Additionally, the antioxidant activity of OVA–TA–KAE–SA was stronger than that of OVA–KAE–SA, indicating that the addition of TA improved the non-covalent binding of KAE and OVA–SA, and enhanced the antioxidant activity, due to the reason that OVA–SA exposed more

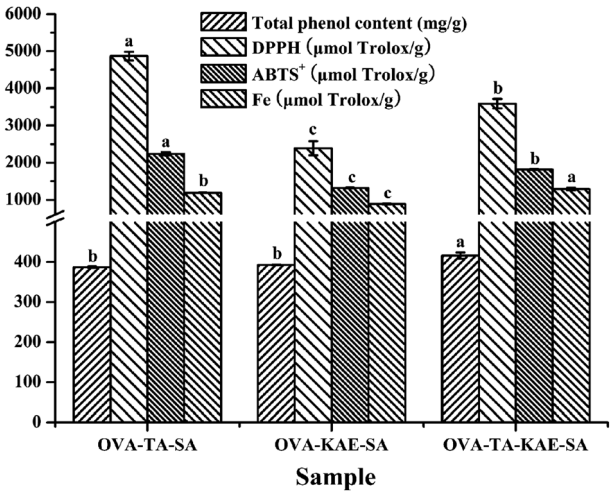

Fig. 6 Total phenol content and antioxidant activities of OVA–SA composite nanoparticles encapsulated KAE/TA. Vertical bars mean standard deviation (SD, $n = 3$). Different letters in the same indicator indicate significant differences at $P < 0.05$.

Table 3 Antimicrobial effect of OVA–SA composite nanoparticles encapsulated KAE/TA[a]

	S. aureus		*E. coli*	
Sample	*D* (mm)	*S* (mm^2)	*D* (mm)	*S* (mm^2)
OVA–TA–SA	25.28 ± 1.15[a]	502.43 ± 46.40[a]	14.90 ± 1.07[a]	175.04 ± 25.56[a]
OVA–KAE–SA	15.07 ± 0.06[c]	177.77 ± 2.04[b]	11.72 ± 0.88[b]	108.32 ± 15.94[b]
OVA–TA–KAE–SA	16.76 ± 0.54[b]	220.74 ± 14.37[b]	13.86 ± 0.49[a]	150.99 ± 10.55[a]
OVA–SA	9.03 ± 0.56[d]	64.19 ± 7.77[c]	7.90 ± 0.42[c]	49.13 ± 5.37[c]
Control	7.50	44.16	7.50	44.16

[a] Values are expressed as mean ± standard deviation. Different letters in the same column indicate significant differences at $P < 0.05$.

hydroxyl groups when TA and KAE were embedded, thus significantly improving the antioxidant capacity of the nanoparticles.[62,63]

3.9. Antibacterial ability

The results of the diameter and area of the growth inhibition zone of *S. aureus* (G+) and *E. coli* (G−) by different composite nanoparticles were shown in Table 3. The antibacterial ability of four composite nanoparticles against *S. aureus* and *E. coli* was OVA–TA–SA > OVA–TA–KAE–SA > OVA–KAE–SA. The antibacterial ability against *S. aureus* was significantly stronger than that against *E. coli*, because the cell wall structure of the Gram-negative bacteria *E. coli* was complex, and contained various proteins, polysaccharides, and peptidoglycans, which became a barrier for hydrophobic substances to enter the bacterial cell, thus the antibacterial effect of hydrophilic TA was better than that of hydrophobic KAE.[64] Whereas the cell wall of the Gram-positive bacteria *S. aureus* had no outer membrane and could be easily penetrated by active compounds with stronger inhibitory effects, resulting the stronger antibacterial ability against *S. aureus*.[65] Additionally, the results of antibacterial ability were in accordance to that of antioxidant assay, because the antibacterial ability of OVA–TA–KAE–SA was significantly enhanced compared with that of OVA–KAE–SA, which means TA plays a more important role than KAE in antioxidant and antibacterial ability.

4. Conclusion

The encapsulation of KAE/TA changed the protein conformation, and increased the system stability and thermal stability of OVA–SA composite nanoparticles. The protein conformation of OVA–TA–SA was the most stable, and the system stability and thermal stability of OVA–TA–KAE–SA were the strongest. Additionally, the composite nanoparticles were endowed with antioxidant activity. OVA–TA–SA had the strongest antioxidant and antibacterial ability. Our findings suggest that OVA–SA composite nanoparticle provides a promising strategy in the delivery of bioactive compounds.

Conflicts of interest

The authors have no conflict of interest.

Acknowledgements

This research was financially supported by the National Key R&D Program of China (2018YFD0901106), the Wenzhou Science and Technology Program (ZN2021002) and the Ningbo "3315 Series Program" for high-level talents (2020B-34-G).

References

1 Q. Liu, Y. Jing, C. Han, H. Zhang and Y. Tian, Encapsulation of curcumin in zein/caseinate/sodium alginate nanoparticles with improved physicochemical and controlled release properties, *Food Hydrocolloids*, 2019, **93**, 432–442.
2 H. Cheng, Z. Fang, T. C. Liu, Y. H. Gao and L. Liang, A study on ss-lactoglobulin-triligand-pectin complex particle: Formation, characterization and protection, *Food Hydrocolloids*, 2018, **84**, 93–103.
3 H. J. Yan, C. Chircov, X. Y. Zhong, B. Winkeljann, I. Dobryden, H. E. Nilsson, O. Lieleg, P. M. Claesson, Y. Hedberg and T. Crouzier, Reversible Condensation of Mucins into Nanoparticles, *Langmuir*, 2018, **34**(45), 13615–13625.
4 L. Y. Chen, G. E. Remondetto and M. Subirade, Food protein-based materials as nutraceutical delivery systems, *Trends Food Sci. Technol.*, 2006, **17**(5), 272–283.
5 O. E. Sponton, A. A. Perez, C. R. Carrara and L. G. Santiago, Impact of environment conditions on physicochemical characteristics of ovalbumin heat-induced nanoparticles and on their ability to bind PUFAs, *Food Hydrocolloids*, 2015, **48**, 165–173.
6 Y. Chen, J. Hu, X. Yi, B. Ding, W. Sun, F. Yan, S. Wei and Z. Li, Interactions and emulsifying properties of ovalbumin with tannic acid, *LWT–Food Sci. Technol.*, 2018, **95**, 282–288.
7 Y. J. Liu, D. Y. Ying, Y. X. Cai and X. Y. Le, Improved antioxidant activity and physicochemical properties of curcumin by adding ovalbumin and its structural characterization, *Food Hydrocolloids*, 2017, **72**, 304–311.
8 J. Feng, H. Cai, H. Wang, C. Y. Li and S. B. Liu, Improved oxidative stability of fish oil emulsion by grafted ovalbumin-catechin conjugates, *Food Chem.*, 2018, **241**, 60–69.
9 C. H. Chang, T. G. Meikle, Y. J. Su, X. T. Wang, C. Dekiwadia, C. J. Drummond, C. E. Conn and Y. J. Yang, Encapsulation in

egg white protein nanoparticles protects anti-oxidant activity of curcumin, *Food Chem.*, 2019, **280**, 65–72.
10 H. Li, Y. Xu, X. Sun, S. H. Wang, J. W. Wang, J. X. Zhu, D. F. Wang and L. L. Zhao, Stability, bioactivity, and bioaccessibility of fucoxanthin in zein-caseinate composite nanoparticles fabricated at neutral pH by antisolvent precipitation, *Food Hydrocolloids*, 2018, **84**, 379–388.
11 L. Jakobek, Interactions of polyphenols with carbohydrates, lipids and proteins, *Food Chem.*, 2015, **175**, 556–567.
12 K. B. Narayanan and S. S. Han, Dual-crosslinked poly(vinyl alcohol)/sodium alginate/silver nanocomposite beads - A promising antimicrobial material, *Food Chem.*, 2017, **234**, 103–110.
13 S. F. Mirpoor, S. M. H. Hosseini and G. H. Yousefi, Mixed biopolymer nanocomplexes conferred physicochemical stability and sustained release behavior to introduced curcumin, *Food Hydrocolloids*, 2017, **71**, 216–224.
14 A. C. Pinheiro, M. A. Coimbra and A. A. Vicente, In vitro behaviour of curcumin nanoemulsions stabilized by biopolymer emulsifiers - Effect of interfacial composition, *Food Hydrocolloids*, 2016, **52**, 460–467.
15 S. Dey and K. Sreenivasan, Conjugation of curcumin onto alginate enhances aqueous solubility and stability of curcumin, *Carbohydr. Polym.*, 2014, **99**, 499–507.
16 A. Magaly Leon, J. M. Aguilera and D. J. Park, Mechanical, rheological and structural properties of fiber-containing microgels based on whey protein and alginate, *Carbohydr. Polym.*, 2019, **207**, 571–579.
17 J. J. Pei, A. Chen, P. Dong, X. J. Shi, L. G. Zhao, F. L. Cao and F. Tang, Modulating heterologous pathways and optimizing fermentation conditions for biosynthesis of kaempferol and astragalin from naringenin in Escherichia coli, *J. Ind. Microbiol. Biotechnol.*, 2019, **46**(2), 171–186.
18 B. X. Li, W. C. Wang, X. P. Zhang, D. X. Zhang, Y. P. Ren, Y. Gao, W. Mu and F. Liu, Using Coordination Assembly as the Microencapsulation Strategy to Promote the Efficacy and Environmental Safety of Pyraclostrobin, *Adv. Funct. Mater.*, 2017, **27**(29), 1701841.
19 J. Serrano, R. Puupponen-Pimia, A. Dauer, A. M. Aura and F. Saura-Calixto, Tannins: Current knowledge of food sources, intake, bioavailability and biological effects, *Mol. Nutr. Food Res.*, 2009, **53**, S310–S329.
20 P. Brouwer, K. G. J. Nierop, W. J. J. Huijgen and H. Schluepmann, Aquatic weeds as novel protein sources: Alkaline extraction of tannin-rich Azolla, *Biotechnol. Rep.*, 2019, **24**, e00368.
21 X. H. Nie, L. M. Zhao, N. N. Wang and X. H. Meng, Phenolics-protein interaction involved in silver carp myofibrilliar protein films with hydrolysable and condensed tannins, *LWT–Food Sci. Technol.*, 2017, **81**, 258–264.
22 E. A. Foegeding, N. Plundrich, M. Schneider, C. Campbell and M. A. Lila, Protein-polyphenol particles for delivering structural and health functionality, *Food Hydrocolloids*, 2017, **72**, 163–173.
23 Y. Song and S. H. Yoo, Quality improvement of a rice-substituted fried noodle by utilizing the protein-polyphenol interaction between a pea protein isolate and green tea (Camellia sinensis) extract, *Food Chem.*, 2017, **235**, 181–187.
24 N. P. Ulrih, Analytical techniques for the study of polyphenol-protein interactions, *Crit. Rev. Food Sci. Nutr.*, 2017, **57**(10), 2144–2161.
25 Y. Chen, Z. Li, X. Yi, H. Kuang, B. Ding, W. Sun and Y. Luo, Influence of carboxymethylcellulose on the interaction between ovalbumin and tannic acid *via* noncovalent bonds and its effects on emulsifying properties, *LWT–Food Sci. Technol.*, 2020, **118**, 108778.
26 J. Feng, H. Xu, L. Zhang, H. Wang, S. Liu, Y. Liu, W. Hou and C. Li, Development of Nanocomplexes for Curcumin Vehiculization Using Ovalbumin and Sodium Alginate as Building Blocks: Improved Stability, Bioaccessibility, and Antioxidant Activity, *J. Agric. Food Chem.*, 2019, **67**, 379–390.
27 J. Gao, C. Liu, J. Shi, F. Ni, Q. Shen, H. Xie, K. Wang, Q. Lei, W. Fang and G. Ren, The regulation of sodium alginate on the stability of ovalbumin-pectin complexes for VD3 encapsulation and *in vitro* simulated gastrointestinal digestion study, *Food Res. Int.*, 2021, **140**, 110011.
28 B. da Silva Soares, C. W. P. de Carvalho and E. E. Garcia-Rojas, Microencapsulation of Sacha Inchi Oil by Complex Coacervates using Ovalbumin-Tannic Acid and Pectin as Wall Materials, *Food Bioprocess Technol.*, 2021, **14**, 817–830.
29 B. d. S. Soares, R. P. Siqueira, M. G. de Carvalho, J. Vicente and E. E. Garcia-Rojas, Microencapsulation of sacha inchi oil (*Plukenetia volubilis* L.) using complex coacervation: Formation and structural characterization, *Food Chem.*, 2019, **298**, 125045.
30 Z. K. Zhang, J. X. Xiao and G. Q. Huang, Pickering emulsions stabilized by ovalbumin-sodium alginate coacervates, *Colloids Surf., A*, 2020, **595**, 124712.
31 H. D. Silva, J. Poejo, A. C. Pinheiro, F. Donsi, A. T. Serra, C. M. M. Duarte, G. Ferrari, M. A. Cerqueira and A. A. Vicente, Evaluating the behaviour of curcumin nanoemulsions and multilayer nanoemulsions during dynamic *in vitro* digestion, *J. Funct. Foods*, 2018, **48**, 605–613.
32 M. Kumari, C. H. Liu and W. C. Wu, Protein moiety in oligochitosan modified vector regulates internalization mechanism and gene delivery: Polyplex characterization, intracellular trafficking and transfection, *Carbohydr. Polym.*, 2018, **202**, 143–156.
33 M. Cao, A. Cao, J. Wang, L. Cai, J. Regenstein, Y. Ruan and X. Li, Effect of magnetic nanoparticles plus microwave or far-infrared thawing on protein conformation changes and moisture migration of red seabream (Pagrus Major) fillets, *Food Chem.*, 2018, **266**, 498–507.
34 Y. Y. Chen, K. Liu, X. Q. Zha, Q. M. Li, L. H. Pan and J. P. Luo, Encapsulation of luteolin using oxidized lotus root starch nanoparticles prepared by anti-solvent precipitation, *Carbohydr. Polym.*, 2021, **273**, 118552.
35 L. Y. Chen, C. W. Cheng and J. Y. Liang, Effect of esterification condensation on the Folin-Ciocalteu method for the quantitative measurement of total phenols, *Food Chem.*, 2015, **170**, 10–15.
36 Y. Gong, Z. Hou, Y. Gao, Y. Xue, X. Liu and G. Liu, Optimization of extraction parameters of bioactive

components from defatted marigold (Tagetes erecta L.) residue using response surface methodology, *Food Bioprod. Process.*, 2012, **90**(1), 9–16.

37 M. Yan, B. Li, X. Zhao and J. Yi, Physicochemical properties of gelatin gels from walleye pollock (Theragra chalcogramma) skin cross-linked by gallic acid and rutin, *Food Hydrocolloids*, 2011, **25**(5), 907–914.

38 T. J. I. Edison and M. G. Sethuraman, Instant green synthesis of silver nanoparticles using Terminalia chebula fruit extract and evaluation of their catalytic activity on reduction of methylene blue, *Process Biochem.*, 2012, **47**(9), 1351–1357.

39 A. A. Perez, R. B. Andermatten, A. C. Rubiolo and L. G. Santiago, Beta-lactoglobulin heat-induced aggregates as carriers of polyunsaturated fatty acids, *Food Chem.*, 2014, **158**, 66–72.

40 Y. Zou, J. Guo, S. W. Yin, J. M. Wang and X. Q. Yang, Pickering Emulsion Gels Prepared by Hydrogen-Bonded Zein/Tannic Acid Complex Colloidal Particles, *J. Agric. Food Chem.*, 2015, **63**(33), 7405–7414.

41 M. Zhou, T. Wang, Q. Hu and Y. Luo, Low density lipoprotein/pectin complex nanogels as potential oral delivery vehicles for curcumin, *Food Hydrocolloids*, 2016, **57**, 20–29.

42 Z. S. Li, Y. T. Wang, Y. Q. Pei, W. F. Xiong, C. L. Zhang, W. Xu, S. L. Liu and B. Li, Curcumin encapsulated in the complex of lysozyme/carboxymethylcellulose and implications for the antioxidant activity of curcumin, *Food Res. Int.*, 2015, **75**, 98–105.

43 X. S. Wu, L. Y. Cai, A. L. Cao, Y. B. Wang, T. T. Lie and J. R. Li, Comparative study on acid-soluble and pepsin-soluble collagens from skin and swim bladder of grass carp (Ctenopharyngodon idella), *J. Sci. Food Agric.*, 2016, **96**(3), 815–821.

44 Y. H. Lin, S. C. Tsai, C. H. Lai, C. H. Lee, Z. S. He and G. C. Tseng, Genipin-cross-linked fucose-chitosan/heparin nanoparticles for the eradication of Helicobacter pylori, *Biomaterials*, 2013, **34**(18), 4466–4479.

45 H. Z. Qiao, M. J. Sun, Z. G. Su, Y. Xie, M. L. Chen, L. Zong, Y. H. Gao, H. P. Li, J. P. Qi, Q. Zhao, X. C. Gu and Q. N. Ping, Kidney-specific drug delivery system for renal fibrosis based on coordination-driven assembly of catechol-derived chitosan, *Biomaterials*, 2014, **35**(25), 7157–7171.

46 Z. Z. Li, S. A. Xu, L. X. Wen, F. Liu, A. Q. Liu, Q. Wang, H. Y. Sun, W. Yu and J. F. Chen, Controlled release of avermectin from porous hollow silica nanoparticles: Influence of shell thickness on loading efficiency, UV-shielding property and release, *J. Controlled Release*, 2006, **111**(1–2), 81–88.

47 H. M. Rawel, S. Rohn, H. P. Kruse and J. Kroll, Structural changes induced in bovine serum albumin by covalent attachment of chlorogenic acid, *Food Chem.*, 2002, **78**(4), 443–455.

48 P. R. Sarika, N. R. James, P. R. A. Kumar, D. K. Raj and T. V. Kumary, Gum arabic-curcumin conjugate micelles with enhanced loading for curcumin delivery to hepatocarcinoma cells, *Carbohydr. Polym.*, 2015, **134**, 167–174.

49 T. Zhang, Y. Xue, Z. J. Li, Y. M. Wang, W. G. Yang and C. H. Xue, Effects of Ozone-Induced Oxidation on the Physicochemical Properties of Myofibrillar Proteins Recovered from Bighead Carp (Hypophthalmichthys nobilis), *Food Bioprocess Technol.*, 2015, **8**(1), 181–190.

50 H. L. Zhou, J. k. Pandya, Y. B. Tan, J. N. Liu, S. F. Peng, J. L. M. Mundo, L. L. He, H. Xiao and D. J. McClements, Role of Mucin in Behavior of Food-Grade TiO_2 Nanoparticles under Simulated Oral Conditions, *J. Agric. Food Chem.*, 2019, **67**(20), 5882–5890.

51 C. J. Cheng, M. Ferruzzi and O. G. Jones, Fate of lutein-containing zein nanoparticles following simulated gastric and intestinal digestion, *Food Hydrocolloids*, 2019, **87**, 229–236.

52 L. Y. Cai, J. H. Feng, A. L. Cao, H. Y. Tian, J. Wang, Y. G. Liu, L. X. Gong and J. R. Li, Effect of Partial Substitutes of NaCl on the Cold-Set Gelation of Grass Carp Myofibrillar Protein Mediated by Microbial Transglutaminase, *Food Bioprocess Technol.*, 2018, **11**(10), 1876–1886.

53 H. J. Yang, W. G. Zhang, T. Li, H. B. Zheng, M. A. Khan, X. L. Xu, J. X. Sun and G. H. Zhou, Effect of protein structure on water and fat distribution during meat gelling, *Food Chem.*, 2016, **204**, 239–245.

54 V. Cabra, R. Arreguin, R. Vazquez-Duhalt and A. Farres, Effect of temperature and pH on the secondary structure and processes of oligomerization of 19 kDa alpha-zein, *Biochim. Biophys. Acta, Proteins Proteomics*, 2006, **1764**(6), 1110–1118.

55 Y. B. Byaruhanga, M. N. Emmambux, P. S. Belton, N. Wellner, K. G. Ng and J. R. N. Taylor, Alteration of kafirin and kafirin film structure by heating with microwave energy and tannin complexation, *J. Agric. Food Chem.*, 2006, **54**(12), 4198–4207.

56 J. Parada and J. M. Aguilera, Food microstructure affects the bioavailability of several nutrients, *J. Food Sci.*, 2007, **72**(2), R21–R32.

57 L. Y. Cai, L. Y. Nian, G. H. Zhao, Y. H. Zhang, L. Sha and J. R. Li, Effect of Herring Antifreeze Protein Combined with Chitosan Magnetic Nanoparticles on Quality Attributes in Red Sea Bream (Pagrosomus major), *Food Bioprocess Technol.*, 2019, **12**(3), 409–421.

58 K. Mackay, P. Papakonstantinou, P. M. Dodd, R. Atkinson and R. J. Pollard, Microstructure, magnetic and nanomechanical properties of FeTaN films prepared by co-sputtering, *J. Phys. D: Appl. Phys.*, 2001, **34**(1), 41–47.

59 Z. Zhang, X. F. Chen, L. Chen, S. J. Yu, Y. Cao, C. L. He and X. S. Chen, Intracellular pH-Sensitive PEG-block-Acetalated-Dextrans as Efficient Drug Delivery Platforms, *ACS Appl. Mater. Interfaces*, 2013, **5**(21), 10760–10766.

60 K. M. Zhang and O. Q. Ni, Rheological Properties and Stability of Highly Concentrated Water-In-Oil Emulsions with Different Emulsifiers, *J. Dispersion Sci. Technol.*, 2015, **36**(4), 549–555.

61 V. Kozlovskaya, B. Xue, W. Q. Lei, L. E. Padgett, H. M. Tse and E. Kharlampieva, Hydrogen-Bonded Multilayers of

Tannic Acid as Mediators of T-Cell Immunity, *Adv. Healthcare Mater.*, 2015, **4**(5), 686–694.

62 H. Shen, C. T. Duan, J. Guo, N. Zhao and J. Xu, Facile *in situ* synthesis of silver nanoparticles on boron nitride nanosheets with enhanced catalytic performance, *J. Mater. Chem. A*, 2015, **3**(32), 16663–16669.

63 F. L. Yen, T. H. Wu, C. W. Tzeng, L. T. Lin and C. C. Lin, Curcumin Nanoparticles Improve the Physicochemical Properties of Curcumin and Effectively Enhance Its Antioxidant and Antihepatoma Activities, *J. Agric. Food Chem.*, 2010, **58**(12), 7376–7382.

64 M. H. Hosseini, S. H. Razavi and M. A. Mousavi, Antimicrobial, Physical and Mechanical Properties of Chitosan-Based Films Incorporated with Thyme, Clove and Cinnamon Essential Oils, *J. Food Process. Preserv.*, 2009, **33**(6), 727–743.

65 M. Ahmad, S. Benjakul, T. Prodpran and T. W. Agustini, Physico-mechanical and antimicrobial properties of gelatin film from the skin of unicorn leatherjacket incorporated with essential oils, *Food Hydrocolloids*, 2012, **28**(1), 189–199.